

## Automatic crater classification framework based on shape parameters

Suchit Purohit<sup>1,\*</sup>, Savita Gandhi<sup>1</sup> and Prakash Chauhan<sup>2</sup>

<sup>1</sup>Department of Computer Science, Gujarat University, Ahmedabad 380 015, India

<sup>2</sup>Indian Institute of Remote Sensing, Indian Space Research Organization, Dehradun 248 001, India

**This communication presents a framework for automatically classifying a crater image into one of its preservation states namely fresh, floor-fractured and degraded introducing a class of algorithms known as crater classification algorithms (CCA). This study involves identification of discriminatory parameters of classes, development and implementation of algorithms to automatically evaluate the parameters from a given Digital Elevation Model testing on representative craters of each class and evolve a decision tree framework for automatically classifying given crater image into its preservation class. This classification can be applied to craters that exhibit ambiguous topographies to test whether they were formed by impact erosion or igneous modification.**

**Keywords:** Classification algorithms, computational intelligence, impact craters, shape parameters.

DUE to the large volumes of data provided by the continuously increasing planetary missions, there is a need for computational advancements in the form of specialized algorithms for various data management, visualization and information extraction tasks. In this view, research in the area of applying computational intelligence to planetary data is gaining attraction of both computer and planetary scientists since the last two decades. Under this domain, the most significant area which is gaining importance is the application of computational intelligence to vastly studied features found on planetary surfaces: impact craters. These are the most significant landforms on the lunar surface. Study of craters and their geomorphology provides important breakthroughs to understand the origin and evolution theories of planetary surfaces. Lunar craters are the most studied craters, the primary reason being their abundance. So far, the development of algorithms with impact craters as the subject is limited to a class of algorithms that automatically detects craters from a given dataset and referred to as crater detection algorithms. Summary of approaches and datasets used in various CDAs has been presented in the literature<sup>1,2</sup>.

This study adds another dimension to algorithms involving craters as the subject of interest. We present an interactive software for automatically classifying a crater

image into one of its preservation states, namely fresh, floor-fractured and degraded, introducing a class of algorithms known as crater classification algorithms (CCA). This study involves identification of crater parameters for discrimination of classes, development and implementation of algorithms to automatically evaluate the parameters from a given digital elevation model, testing on representative craters of each class and developing decision tree framework for automatically classifying a given crater image to its class. This classification can be applied to craters that exhibit ambiguous topographies to test whether they were formed by impact erosion or igneous modification.

Craters differ from each other in terms of morphology, age, composition and origin. Several classification schemes have been proposed to differentiate between the craters. Table 1 summarizes various classification schemes involving the criteria used, number and name of classes. Though there are many classification schemes proposed, none of them involves a special class of igneously modified craters known as floor-fractured craters (FFCs). Moreover, the morphological descriptions used in the schemes are qualitative resulting in subjective classification. Hence, this study proposes a classification system based on quantitative description of crater morphology to discriminate craters based on their preservation/modification states into three classes, namely fresh, floor-fractured and degraded. Fresh craters are the youngest, created from impacts that occurred within the last 1–2 billion years. They are referred to as Copernican craters formed during the Copernican age, which is the youngest of all geologic periods of lunar surfaces. They have experienced no modifications in topography and have well-pronounced sharp features. These craters are bowl-shaped, deep, have sharp rims and display bright white, high-albedo rays made up of ejecta and debris from their formation<sup>3</sup>. The degraded class comprises craters formed due to impacts that occurred more than 3 billion years ago. Compared to the fresh craters, degraded craters exhibit reduced/dull topography. The erosion process on the lunar surface is responsible for transformation of fresh craters into degraded ones. The only form of erosion acting on lunar craters are solar winds and formation of other craters in the surrounding areas. This degradation process affects nearly all the parameters, the most prominent one being depth. They are characterized by shallow floors because the repeated ejecta spray, discharged by nearby impacts, fills the interiors making them shallower and flat. They are characterized by diminished rims, with reduced flank and rim height as a result of subsequent cratering processes. Diameter is the one parameter that generally exhibits insignificant changes during the degradation process<sup>4</sup>. Lunar FFCs are a particular class of craters characterized by shallow plate-like floors with fractures of various depths and orientations like radial, concentric or polygonal, and exhibit additional

\*For correspondence. (e-mail: suchit.s.purohit@ieee.org)

**Table 1.** Summary of classification schemes

Refs	Criterion	No. of classes
12	Shape	Four – Simple bowl-shaped, uplifted, flat-based, concentric.
13	Rim diameter	Four – Simple, complex, peak ring basins, multiring basins.
14	Shape and diameter	Seven – Simple, bowl-shaped, flat-based, central-uplifted, concentric, complex and lunar mare remnant.
15	Clarity of boundaries	Five – Clearly visible to barely visible.
16		13 types of craters, 23 types of ring structures.
Nakano, 1970	Spatial patterns and crater scale	7 primary, 13 atypical types of lunar impact craters.
17	Crater margin, wall structure and floor type	18 types further sub-divided into 5 types based on degree of erosion.

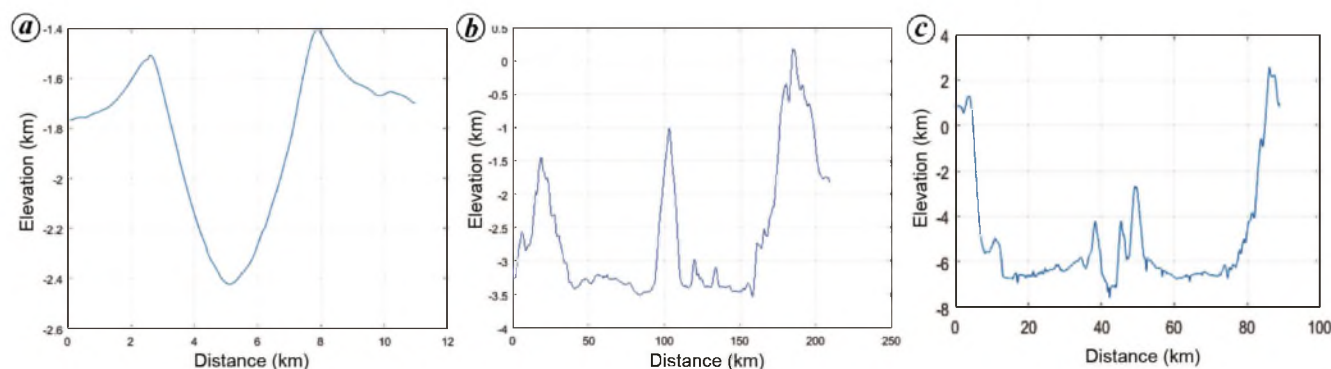


**Figure 1.** Altimetry profiles: (a) fresh, (b) degraded and (c) floor-fractured craters.

interior features like moats, ridges, pits of mare material and dark-holed pits<sup>5</sup>. The past geologic activity on the moon has accounted for these fractures and cracks. The magma produced by the moon when it was still geologically active, was collected under impact craters and began to swell underneath the floors of the craters. The floors were pushed up by magma causing cracks in them. On the basis of morphology, Schultz grouped FFCs into six classes and documented distribution of floors over the lunar surface<sup>5</sup>. The FFC distribution was further examined by Jozwiak *et al.* using Lunar Orbital Laser Altimetry (LOLA) data, providing a global mapping of FFCs in their various classes; class 4 was sub-categorized as 4a, 4b, 4c (ref. 6). Figure 1 shows altimetry profiles of craters of the three classes.

An impact crater is formed due to the hyper-velocity impact of a solid celestial body on a planetary surface. Thus, the shape and size of craters depend upon various aspects like size of impactor, angle of impact, intensity of impact and density of the crust. However, the post-impact morphological modifications are controlled by the effect of space weathering, late-stage volcanism, subsurface magmatic activity, mass wasting, etc. These events have effects on morphology and topography of the crater, like decrease in depth-to-diameter ratio, modifications of the crater rim and eventually the shape of the crater. Mass wasting tends to erase surface topographic differences, whereas continuous space weathering results in degradation of a crater’s rim, and reduced depth-to-diameter ratio

of the crater. Post-impact events occurring nearby or overlapping a crater cause variation in elevation of the crater’s boundary, making it irregular. In FFCs, magma pushing resulting in floor upliftments causes reduction in depth-to-diameter ratio while retaining variations in rim height.

Pike found that a strong correlation exists between diameter and depth for fresh craters, which exhibited a linear trend on log–log plot. The correlation equation is given by  $d = aD^b$ , where  $d$  is the depth of crater (km),  $D$  the diameter of the crater (km)  $a = 1.044$  and  $b = 0.301$  for craters >15 km in diameter<sup>3</sup>. This can be used as a basis to examine whether other types of lunar craters also exhibit trends unique enough to differentiate among the three types.

Based on the aforementioned facts, the parameters that allow separation of FFCs from the other two classes were identified as depth-to-diameter ratio and those parameters quantising rim degradation degree, namely measures of elongation of boundary ( $S_2$ ); lumpiness of rim ( $S_3$ ); roughness of elevation ( $R_e$ ) and roughness of radii ( $R_r$ )<sup>7</sup>.

The following methodology was used. (1) End-members of each class were identified. They were binned according to various ranges of diameter, i.e. 28–33, 40–42, 85–112 and 160–200 km. End-members are considered exemplary for their class because they contain majority of the characteristics for their specific class. Jozwiak *et al.*<sup>6</sup> identified Humboldt, Vitello, Gassendi and Gaudibert craters as end-members for the floor-fractured class. Craters

from fresh and degraded class were selected such that they are of comparable in diameter and spatially correlated to selected FFCs. Accordingly, Tycho, Glushko, Hausen and Kepler were identified as fresh counterparts of FFCs and Hess, Asclepi, Richardson and Daedalus U were identified as degraded craters. We referred to the work of Losaik *et al.*<sup>8</sup> for determining diameter and geological ages of selected craters.

(2) The morphometric parameters of craters like diameter, depth, rim height and rim width were determined using an in-house program developed by the present authors, which automatically determines morphometric parameters from a given digital elevation model (DEM) of a crater<sup>9</sup>.

(3) Algorithms for determination of parameters quantifying rim quality were developed (Figure 2). They were implemented in MATLAB environment and tested for selected craters. Based on value of parameter combinations from steps 2 and 3, a decision tree-based classification framework was developed.

Before extraction of parameters, crater boundary must be determined. The algorithm for rim delineation is described using steps (i)–(v) below. Figure 3 depicts various stages of execution of the algorithm on DEM of TYCHO crater. (i) Apply  $5 \times 5$  mask ( $M$ ) centred over each pixel ( $i, j$ ) of the crater's DEM image and calculate its local mean ( $m$ ) value. (ii) Find the greatest deviation from local mean ( $m$ ) to the minimum ( $M_{\min}$ ) or maximum ( $M_{\max}$ ) of the values in the mask according to eq. (1) and store in image  $A$ .

$$A[i, j] = \text{maximum}((m - M_{\min}), (M_{\max} - m)). \quad (1)$$

(iii) Find the threshold value ( $T$ ) to generate a binary image.

$$T = \alpha \times [A_{\max} - A_{\min}] + A_{\min}, \quad (2)$$

where  $\alpha = 0.25$  is the empirical value,  $A_{\min}$  the minimum pixel value of  $A$  and  $A_{\max}$  is the maximum pixel value of

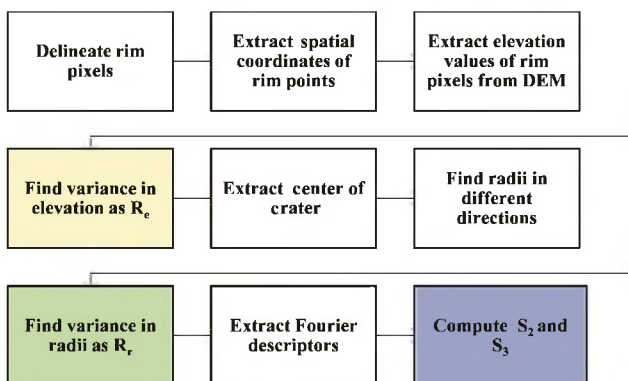


**Figure 2.** Steps for extraction of  $S_2$  measurement of elongation;  $S_3$ , measurement of lumpiness;  $R_e$ , Roughness of elevation and  $R_r$ , roughness of radii.

(iv) To smoothen the edges and eliminate small holes in the binary image, apply morphological closing with  $3 \times 3$  structure element. (v) Apply thinning operation to the resulting binary image to decrease the lines into a single pixel thickness. These single pixels are regarded as rim pixels.

Steps no. (i) to (v) above describe the process of centre point extraction and computing of radii in different directions. Figure 4 illustrates output of various stages of the process. (i) Extract index value and elevation values of each rim pixel from DEM. (ii) Fit the rim/boundary to a circle. Find radius of circle ( $r$ ) and centre ( $X_C, Y_C$ ). (iii) Convert Cartesian coordinates of rim pixels into polar coordinates as

$$X = (r \times \cos(\theta)) + X_C, \quad (3)$$

$$Y = (r \times \sin(\theta)) + Y_C, \quad (4)$$

(iv) Repeat step (iii) varying  $\theta$  from  $0^\circ$  to  $360^\circ$  to obtain 360 rim pixels on the boundary and find radius of the circle at each rim pixel using the distance formula:

$$R_i = [(Y_C - Y_i)^2 + (X_C - X_i)^2]^{1/2}, \quad (5)$$

where ( $X_i, Y_i$ ) are rim pixels of varying angular displacements from  $0^\circ$  to  $360^\circ$  and  $R_i$  is the radius of the crater at each rim pixel.

In order to extract lumpiness and elongation parameters of the crater rim, Fourier expansion was used<sup>7</sup> (the detailed analysis of Fourier expansion and its use in determining shape is out of scope of this study). The algorithm used is as follows:

(i) Fourier expansion is calculated as:

$$a_q = \sum_{i=0}^{360} \sin(q \times \theta_i) / 360, \quad (6)$$

$$b_q = \sum_{i=0}^{360} \cos(q \times \theta_i) / 360, \quad (7)$$

where  $a_q$  and  $b_q$  are Fourier descriptors and  $\theta_i$  is the polar angle of each point ( $X_i, Y_i$ ) given by

$$(\theta_i) = a \tan((Y_i - Y_C) / (X_i - X_C)), \quad (8)$$

where ( $X_C, Y_C$ ) are the coordinates of the centre.

(ii) The elongation  $S_2$  and lumpiness  $S_3$  are computed by substituting  $q = 2$  and  $3$  in eqs (6) and (7) respectively.

$$S_2 = \sqrt{a_2^2 + b_2^2}; \quad S_3 = \sqrt{a_3^2 + b_3^2}. \quad (9)$$

We, next determined roughness of elevation and radius.

(i) The elevation ( $E_i$ ) of each point ( $X_i, Y_i$ ) on the crater's boundary can be obtained from LOLA DEM (Figure 5).

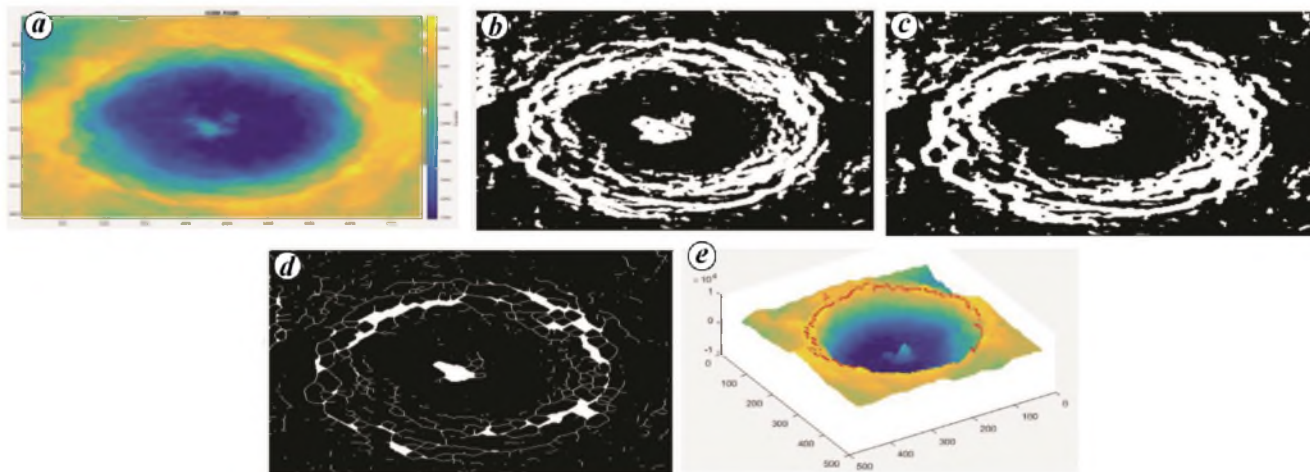


**Figure 3.** Stages of the algorithm for rim delineation. *a*, Original DEM of TYCHO crater; *b*, Binary image; *c*, Closing image; *d*, Thinning image output; *e*, 3D image with rim extraction.

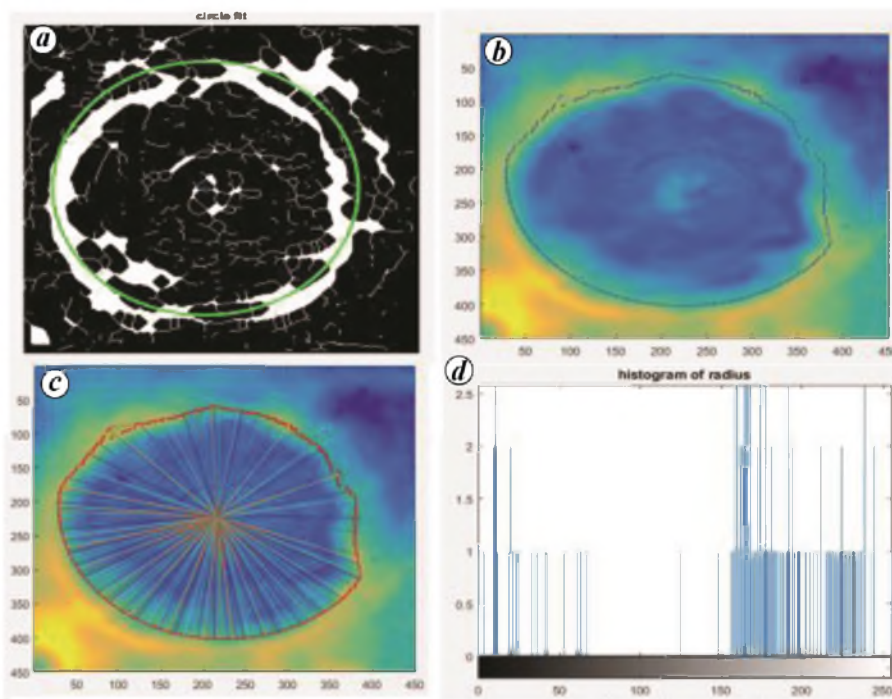


**Figure 4.** Determination of radii in different directions. *a*, Circle fit on vitello crater thinning image; *b*, Maximum elevation points in 0–360 direction; *c*, Centre point, boundary points and radius in 0–360 direction; *d*, Histogram of radius value in 0–360 direction.

The radius  $R_i$  of every point  $P_i$  in the crater’s boundary is obtained from eq. (5). (ii) Compute grey-level histogram for radius and elevation value of rim pixels. (iii) The radius and elevation roughness of a crater are calculated using second moments of histogram

$$R_o/R_r = 1 - (1/(1 + \sigma^2(z))), \tag{10}$$

where  $z$  is a random variable denoting grey-level histogram with levels = 255.

In this study, we used gridded data which are map-projected DEMs derived from altimetry data acquired by LOLA instruments. Datasets pertaining to selected craters were downloaded from the lunar orbital data explorer, PDS geoscience node<sup>10</sup>. These were of resolution 1024 PIX/DEG or 30 m. The measurements in pixel units were converted into distance units using MAP\_SCALE and scaling factor available in the label file of the datasets (ode.rsl.wustl.edu/moon). Scaling factor of 0.5 was used to convert elevation values in pixels to kilometres.

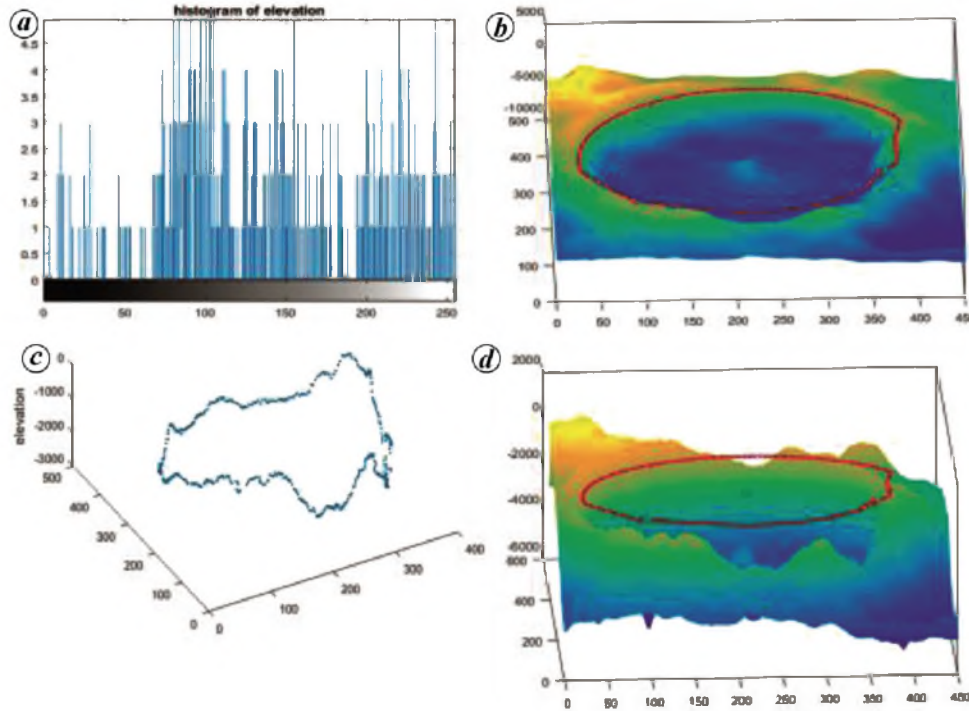


**Figure 5.** Depiction in variance of elevation along boundary points. *a*, Histogram of elevation value in 0–360 direction; *b*, Boundary point on 3D view of centre; *c*, Elevation variation of boundary point; *d*, Boundary point on 3D view of crater.

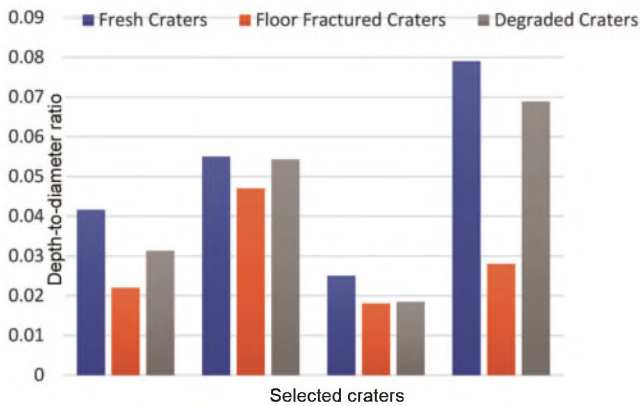


**Figure 6.** Depth-to-diameter ratio plot of selected craters.

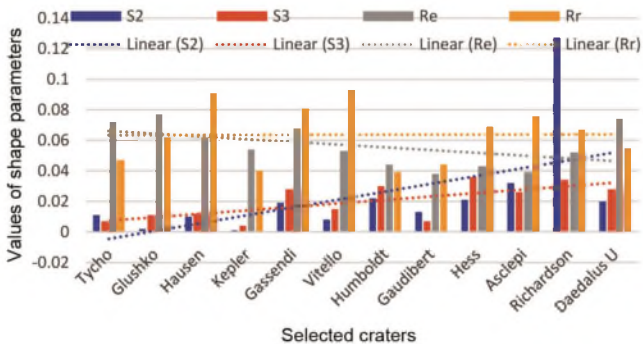


**Figure 7.** Values of shape parameters for selected craters.

$$E(\text{km}) = (E(p) * \text{scaling factor}) / 1000, \quad (11)$$

where  $E(\text{km})$  is the elevation in kilometers and  $E(p)$  is the elevation in pixels.

For horizontal distance,  $\text{MAP\_SCALE} = 0.0296126469$   $\langle \text{km/pix} \rangle$  was used to get distance value in kilometres.

$$D(\text{km}) = D(p) * \text{MAP\_SCALE}, \quad (12)$$

where  $D$  (km) is the distance in kilometres; and  $D(p)$  is the distance in pixels.

The algorithms for determining the parameters were implemented in MATLAB (version R2016b) using mapping, image processing and TOPO toolboxes. The programs were executed on a workstation with 12 GHz internal RAM and processor Intel core i7 CPU with 3.60 GHz speed. The proposed techniques were tested on selected craters from all the three classes. Results are summarized in Table 2, and illustrated in Figures 6 and 7.

As illustrated in Figure 6, for all diameter ranges depth-to-diameter ratio ( $d/D$ ) is maximum for fresh craters and minimum for FFCs. This gives strong evidence that  $d/D$  can provide a clear-cut boundary between fresh craters and other two classes. On comparing the  $d/D$  values across diameter ranges, we found it to be minimum for maximum diameter range. This is expected as with the increasing diameter, the floor flattens reducing the depth<sup>11</sup>. At the same time, if reduction in depth due to

**Table 2.** Values of parameters for selected craters

Class	Crater	Diameter	Age	$S_2$	$S_3$	$R_e$	$R_r$	$d/D$
FRESH	Tycho	85.290	Copernican	0.011	0.007	0.072	0.047	0.0416
	Glushko	40.100	Nectarian	0.002	0.011	0.077	0.062	0.055
	Hausen	163.240	Eratosthenian	0.010	0.012	0.062	0.091	0.025
	Kepler	27.330	Copernican	0.001	0.004	0.054	0.040	0.079
FFC	Gassendi	111.390	Nectarian	0.019	0.028	0.068	0.081	0.022
	Vitello	42.510	Lower Imbrian	0.008	0.015	0.053	0.093	0.047
	Humboldt	199.460	Upper Imbrian	0.022	0.030	0.044	0.039	0.018
	Gaudibert	33.140	Nectarian	0.013	0.007	0.038	0.044	0.028
Degraded	Hess	90.440	Pre-Nectarian	0.021	0.036	0.043	0.069	0.03128
	Asclepi	40.560	Pre-Nectarian	0.032	0.026	0.039	0.076	0.054289
	Richardson	162.560	Pre-Nectarian	0.127	0.034	0.052	0.067	0.01844
	Daedalus U	28.820	Pre-Nectarian	0.020	0.028	0.074	0.055	0.068875

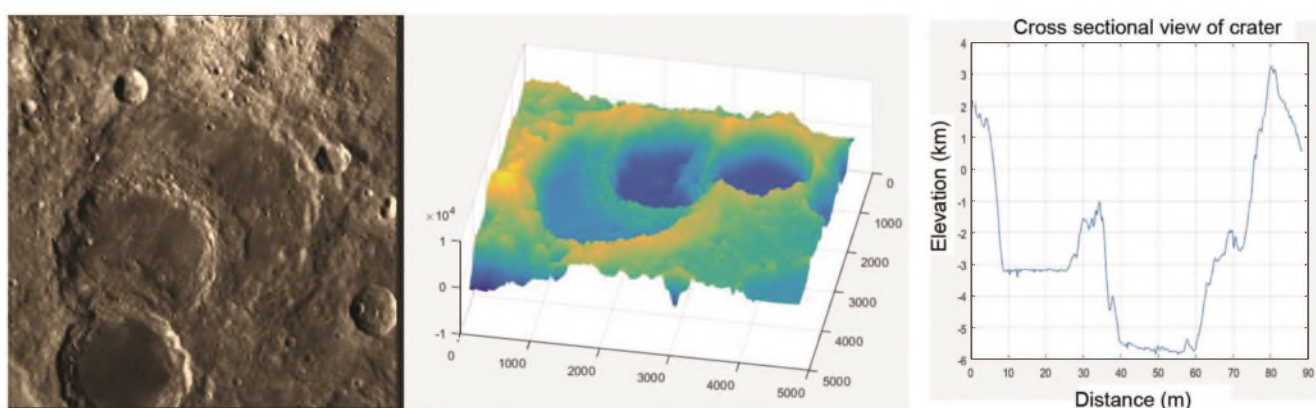


**Figure 8.** LROC image, topographic profile and 3D plot of Richardson crater.

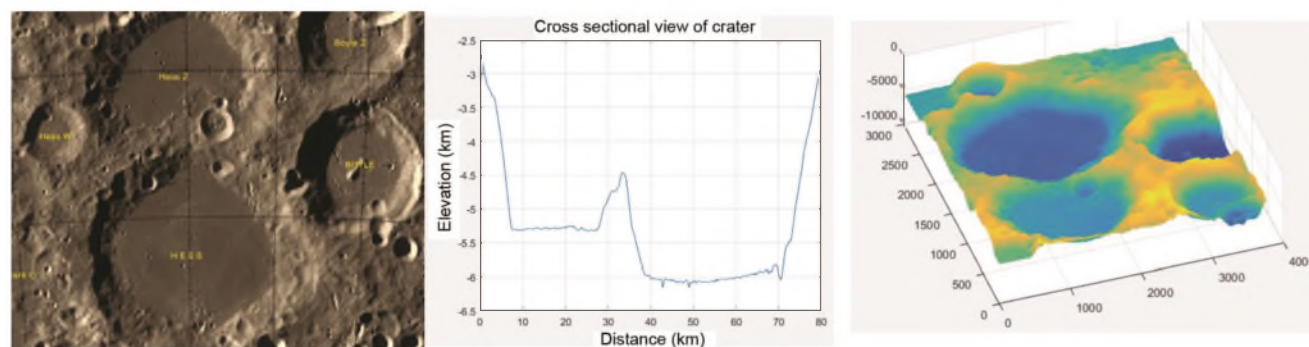


**Figure 9.** LROC image, topographic profile and 3D plot of Hess crater.

post-modification effects is considered, we can conclude that craters with larger diameter are affected the most. Figure 7 plots values of  $S_2$ ,  $S_3$ ,  $R_e$  and  $R_r$  for individual craters and their linear trend across three classes. It can be seen that under each diameter category,  $S_2$  and  $S_3$  are found to be maximum for the degraded class. This is indicative of the fact that degraded craters are subjected to more post-impact modifications, which lead to elongation and lumpiness of boundary of the craters in due course of

time. Elongation of boundary may also be due to oblique impacts, but it is a rare event and cannot be generalized. Amongst all the craters,  $S_2$  was found to be maximum for Richardson crater. A substantial portion of this crater is overlain by Maxwell, which lies across the rim to the southwest and hence in effect providing an elongated boundary (Figure 8).  $S_3$  was found to be maximum for Hess crater. This is because the crater rim has worn out due to subsequent impacts, increasing its lumpiness. The

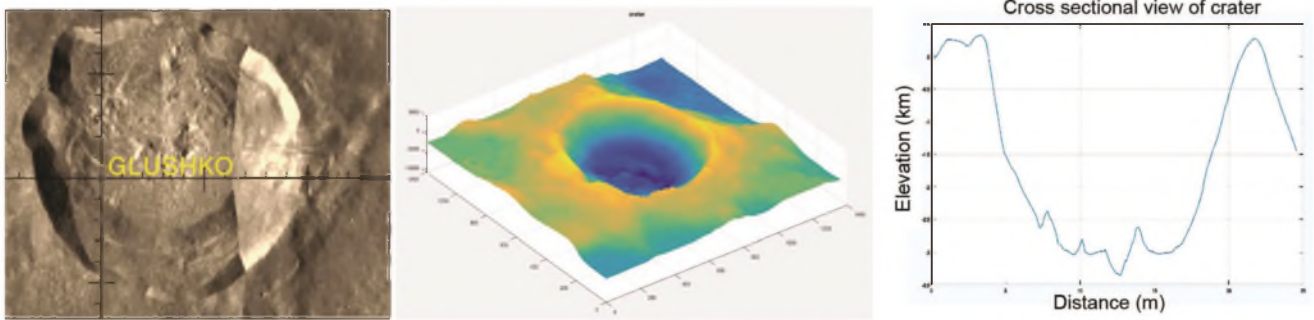


Figure 10. LROC image, topographic profile and 3D plot of Glushko crater.

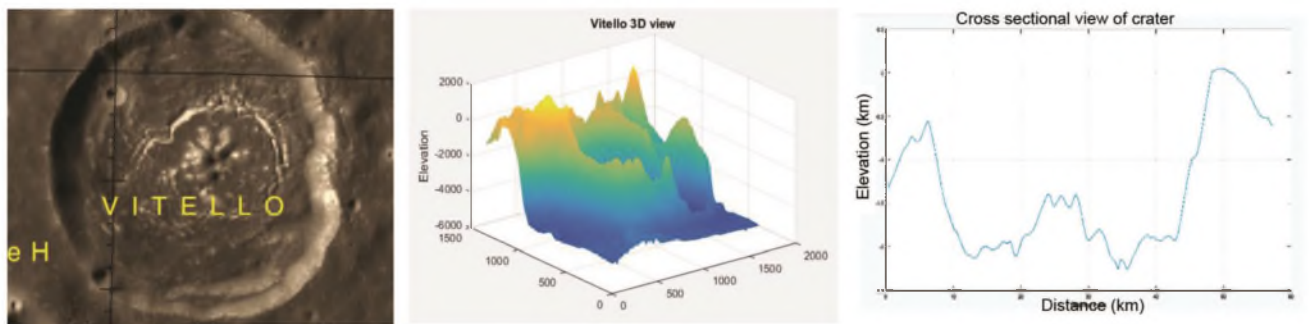


Figure 11. LROC image, topographic profile and 3D plot of Vitello crater.

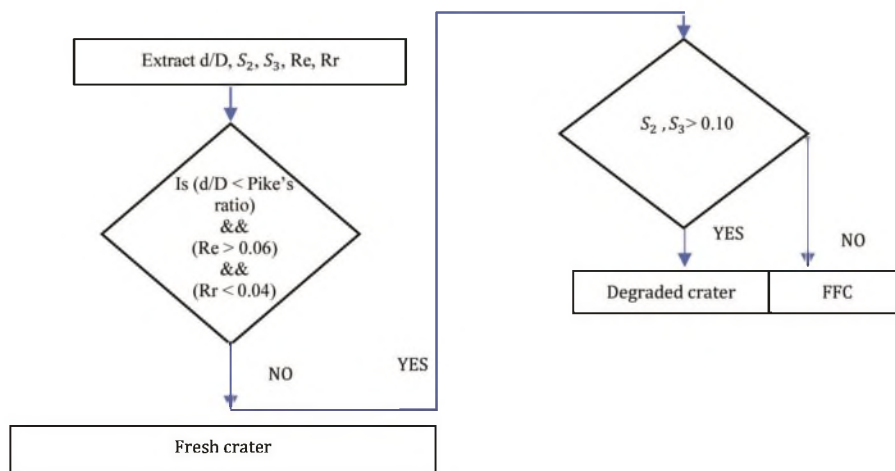


Figure 12. Decision tree framework.

Boyle crater is attached to the northeastern rim of Hess. The satellite crater Hess Z is overlaid by the northern rim of Hess (Figure 9).  $R_e$  parameter signifies the variance in elevation values. Due to space weathering process or secondary impacts, elevation variations are erased and invisible. Therefore, degraded craters are expected to have lower values of  $R_e$ . Our results are found to be consistent with this theory in sense that except for craters in the 27 km category,  $R_e$  was maximum for fresh craters. In the 27 km category of craters,  $R_e$  was found to be maximum

for Daedalus U, belonging to the degraded category. On comparing all the craters, we found  $R_e$  to be maximum for Glushko crater. This crater possesses a sharp, well-defined feature that combined with its higher albedo, are indicative of a relatively young impact crater (Figure 10).  $R_r$  signifies the variance of radius in different directions leading to deformed shape. We did not get a complete biased  $R_r$  value for any particular class, though it is expected to be more for the degraded class.  $R_r$  was found to be maximum for Vitello. That is contributed due to

drastic variations in elevations of left and right rim of the crater (Figure 11).

It can be concluded that depth–diameter ratios of floor-fractured and degraded craters are less than fresh craters. It was also found that these ratios for fresh craters are consistent with Pike’s relation. Therefore, a primary decision can be to evaluate  $d/D$ , and compare it with Pike’s relation. If the ratio is low, the crater can be categorized as belonging to either floor-fractured or degraded class. The rim degradation parameters can then be used to provide the next level of discrimination. Currently, the empirical values have been decided based on analysis of these 12 craters (Table 2). Values of parameters for selected craters only and are as follows:  $R_e = 0.06$ ,  $R_r = 0.04$ ,  $S_2 = 0.10$ ,  $S_3 = 0.10$ . Figure 12 depicts the decision tree framework based on this analysis.

Thus, an automatic classification framework to classify craters according to their post-impact modification states is proposed in this study. We can conclude that parameters depth-to-diameter ratio of the craters, elongation and lumpiness and variance of elevations of crater boundary and variance of radius in different directions are good separators among the crater three classes. Our program could automatically derive the discriminative parameters accurately and rapidly. A decision tree framework based on empirical values of parameters has been proposed. The empirical values are based on the present observations only. Our future work would focus on testing the programs on a greater number of craters and obtain more generic values of discriminative parameters.

1. Salamunićar, G. and Lončarić, S., Open framework for objective evaluation of crater detection algorithms with first test-field subsystem based on MOLA data. *Adv. Sp. Res.*, 2008, **42**(1), 6–19.
2. Gandhi, S. and Suchit, P., Automatic crater detection techniques: a chronological survey. *Int. J. Res. Comput. Sci. Inf.*, 2013, **2**(2(A)), 207–213.
3. Pike, R. J., Crater dimensions from Apollo data and supplemental sources. *Earth. Moon. Planets*, 1976, **15**(3), 463–477.
4. Head, J. W., Processes of lunar crater degradation: Changes in style with geologic time. *The Moon*, 1975, **12**(3), 299–329.
5. Schultz, P. H., Floor-fractured lunar craters. *Earth. Moon. Planets*, 1976, **15**(3), 241–273.
6. Jozwiak, L. M., Head, J. W., Zuber, M. T., Smith, D. E. and Neumann, G. A., Lunar floor-fractured craters: Classification, distribution, origin and implications for magmatism and shallow crustal structure. *J. Geophys. Res. E Planets*, 2012, **117**(11).
7. Li, B., Ling, Z. C., Zhang, J., Wu, Z. C., Ni, Y. H. and Chen, J., The shape and elevation analysis of lunar crater’s true margin. In Lunar and Planetary Science Conference, Texas, 2015, vol. 46, p. 1709.
8. Losiak, A., Kohout, K., Sullivan, K. O., Thaisen, K. and Weider, S., Lunar impact crater database. Lunar Explor. Summer Intern Progr. Lunar Planet. Inst., Texas, 2008.
9. Purohit, S., Gandhi, S. R. and Prakash, C., A novel framework for automatic determination of morphometric parameters of lunar floor-fractured craters. *Planet. Space Sci.*, 2018.
10. Smith, D. E. *et al.*, The lunar orbiter laser altimeter investigation on the lunar reconnaissance orbiter mission. *Space Sci. Rev.*, 2010, **150**(1–4), 209–241.

11. Melosh, H. J., Impact cratering: A geologic process. Oxford Univ. Press (Oxford Monogr. Geol. Geophys. No. 11), 1989, vol. 11, p. 253.
12. Oberbeck, V. R. and Quaide, W. L., Genetic implications of Lunar regolith thickness variations. *Icarus*, 1968, **9**(1–3), 446–465.
13. Stoffler, D., Cratering history and lunar chronology. *Rev. Mineral. Geochem.*, 2006, **60**(1), 519–596.
14. Chen, M., Lei, M., Liu, D., Zhou, Y., Zhao, H. and Qian, K., Morphological features-based descriptive index system for lunar impact craters. *ISPRS Int. J. Geo-Information*, 2017, **7**(2), 5.
15. Baldwin, R. B., *The Face of the Moon*, University of Chicago Press, Chicago, 1949.
16. Fielder, G., *Lunar Geology*, Lutterworth Press, London, 1965.
17. Wood, C. A. and Anderson, L., New morphometric data for fresh lunar craters. In Lunar and Planetary Science Conference Proceedings, 1978, vol. 9, pp. 3669–3689.

ACKNOWLEDGEMENTS. We thank the Indian Space Research Organisation (ISRO) for financial support under the grant ISRO/SSPO/Ch-1/2016-17. We also thank Space Applications Centre, ISRO, Ahmedabad for providing expertise, technical and logistical support throughout this study.

Received 21 February 2018; revised accepted 30 June 2018

doi: 10.18520/cs/v115/i7/1351-1358

## Identification of weather events from INSAT-3D RGB scheme using RAPID tool

A. K. Mitra<sup>1</sup>, Shailesh Parihar<sup>1</sup>, R. Bhatla<sup>2</sup> and K. J. Ramesh<sup>1</sup>

<sup>1</sup>National Satellite Meteorological Centre,  
India Meteorological Department, New Delhi 110 003, India  
<sup>2</sup>Banaras Hindu University, Varanasi 221 005, India

**Real-time analysis of products and information dissemination (RAPID), a web-based quick visualization and analysis tool for INSAT satellite data has been presented for identification of weather events. The combination of channels using red–green–blue (RGB) composites of INSAT-3D satellite and its physical significant value content is presented. The solar reflectance and brightness temperatures are the major components of this scheme. The shortwave thermal infrared (1.6  $\mu\text{m}$ ), visible (0.5  $\mu\text{m}$ ) and thermal IR channels (10.8  $\mu\text{m}$ ) representing cloud microstructure is known as Day Microphysics (DMP) and the brightness temperature (BT) differences between 10.8, 12.0 and 3.9  $\mu\text{m}$  is referred to as Night Microphysics (NMP). The thresholds technique have been developed**

\*For correspondence. (e-mail: ashim\_mitra@rediffmail.com)